Korean J. Chem. Eng., 38(6), 1129-1138 (2021)
DOI: 10.1007/s11814-020-0709-9

pISSN: 0256-1115
eISSN: 1975-7220

Dehydrogenation of ethane and subsequent activation of CO_2 on hierarchically-structured bimetallic FeM@ZSM-5 (M=Ce, Ga, and Sn)

Min Hye Jeong‡, Kyung Soo Park‡, Dong Ming Shen‡, Ji Won Moon, and Jong Wook Bae†

School of Chemical Engineering, Sungkyunkwan University (SKKU),
2066 Seobu-ro, Jangan-gu, Suwon, Gyeonggi-do 16419, Korea
(*Received 29 September 2020 • Revised 6 November 2020 • Accepted 7 November 2020*)

Abstract−The catalytic activity for dehydrogenation of C_2H_6 and successive CO_2 activation was studied by using hierarchically-structured bimetallic FeM/ZSM-5 (M=Ce, Ga, and Sn metal) to verify the redox property of the Fe nanoparticles and metal promoters on the acidic ZSM-5. Based on the surface characteristics, the reducibility and oxygen vacant sites of metal oxides on the ZSM-5 largely altered the reduction-oxidation nature and catalytic cracking behavior. The metal-promoted Fe/ZSM-5, especially with CeO_2 promoter on the FeCe/ZSM-5, revealed excellent redox cycles and higher steady-state dehydrogenation activity such as a comparable C_2H_6 conversion of 6.1% as well as C_2H_4 selectivity of 89.8% at 600 °C with a larger CO production with 9.7 mmol/g by CO_2 activation at 700 °C. This observation was attributed to the incorporated partially reducible CeO_2 species by enhancing their interaction with ZSM-5 as well as by easily stabilizing the oxidation states of Ce and Fe metal oxides with its higher thermal stability during C_2H_6 dehydrogenation through an initial oxidative dehydrogenation followed by a steady-state catalytic cracking and subsequent CO_2 activation to CO.

Keywords: Dehydrogenation of C_2H_6, CO_2 Activation, Redox Cycles of Fe Nanoparticles, ZSM-5, Chemical Looping (CL) Application

INTRODUCTION

Unsaturated hydrocarbons such as olefins and aromatics have been the valuable and versatile chemical building blocks for the subsequent production of polymers, solvents, fuel additives, and chemical intermediates [1]. The increasing shale gas production has caused tremendous changes by utilization of its abundant ethane feedstock [2] with lower price and by competing with oil feedstock [3]. Steam cracking of ethane and naphtha is commercially available industrial process to produce olefin and other hydrocarbons by less controllable radical reactions [4], where the highly endothermic reaction still has many challenges [5] to reduce higher energy demand (<16 GJ/ton ethylene) [6], environmental problems with both CO_2 and NO_x emissions [7], and periodic reactor shutdown due to its severe deactivation nature by coke depositions. Therefore, alternative oxidative dehydrogenation (ODH) of ethane has been investigated often since it can overcome those disadvantages with a comparable ethylene yield on the various mixed metal oxides; however, some practical drawbacks like larger CO_x formation with higher operating cost are still unsolved due to the expensive air separation unit required [2a,8].

To solve those issues of the ODH reaction by co-feeding of ethane with oxygen, we previously proposed a successive two-step chemical looping (CL)-based oxidative dehydrogenation (CL-ODH). The CL-ODH process is composed of an oxidative dehydrogenation of ethane (C_2H_6) to ethylene (C_2H_4) by using active surface lattice oxygens on various mixed metal oxides (reduction step) and subsequently oxidation of the reduced metal oxides by CO_2 activation to CO (oxidation step) following the typical Mars-van Krevelen redox mechanism [9] to complete reduction-oxidation cycles of mixed metal oxides. The utilization of CO_2 as an oxidizing agent can be also helpful to minimize climate change, ocean acidification, and coke formation [10]. The coke precursors generated by the ODH reaction of C_2H_6 can be eliminated by reverse Boudouard reaction ($CO_2+C\rightarrow 2CO$) [11] during the oxidation step with CO_2. The CL-ODH process offers much lower CO_2/NO_x emission with reduction of ~87% compared to the steam cracking reaction [12]. Therefore, it seems to be important to design compatible catalysts for the CL-ODH reaction and recent works have shown the solid acid zeolite applications for the conversion of alkanes to alkenes. Based on DFT calculation [13], the Fe-supported ZSM-5 appears to be a promising catalyst for ethane dehydrogenation due to its lower activation energy on the reduced iron oxide surfaces due to stronger acidic sites of zeolites. The incorporation of metal cations into zeolite frameworks has been proposed to create more active sites for alkane transformation toward olefins [14]. The C-H bond cleavages are more favorable due to its polarization induced between exchanged metal cations and basic oxygen atoms of zeolite frameworks [15]. For example, the Fe sites isolated in the frameworks over the Fe-substituted ZSM-5 were reported to be main active sites for propane dehydrogenation over FeZSM-5 with its modest conversion of ~3.6% and higher propylene selectivity of 78-85% [16].

†To whom correspondence should be addressed.
E-mail: finejw@skku.edu
‡The authors of M.H. Jeong, K.S. Park and D.M. Shen contributed equally.

Furthermore, the basic Sn oxides on the PtSn/ZSM-5 enhanced the transfer of coke precursors on the active sites to the ZSM-5 surfaces possessing 10-membered ring (10-MR) channels, which eventually improved the catalytic stability for propane dehydrogenation [17].

Those characteristics of zeolites with proper transition metals such as the reducible Fe and Ce, Ga oxides can be an alternative to industrial alkane dehydrogenation catalysts (e.g., precious Pt or Cr metal). In the present study, the roles of Fe and metal oxide promoters on the FeM@ZSM-5 (M=Ce, Ga and Sn promoter) with the hierarchically-structured ZSM-5 were explained in terms of its reduction-oxidation natures with steady-state catalytic cracking activity for C_2H_6 dehydrogenation and oxygen vacant sites with its contributions for CO_2 activation to CO.

EXPERIMENTAL SECTION

1. Catalyst Preparation and Activity Measurement for Reduction-oxidation Reaction

An aqueous suspension of silica colloids (Ludox As-40) was first dissolved in ethanol under vigorous stirring, and stoichiometric amounts of $Fe(NO_3)_3{\cdot}9H_2O$ and metal promoters (M) such as $Ga(NO_3)_3{\cdot}xH_2O$, $Ce(NO_3)_3{\cdot}6H_2O$ and $SnCl_3{\cdot}2H_2O$ precursor at a fixed Fe/M molar ratio of ~10 were separately added above the solution for 10 h at room temperature slowly. As-prepared FeM-SiO_2 composites were dried again at 120 °C and then calcined at 400 °C for 4 h at a controlled ramping rate of 1 °C/min. The hierarchically-structured bimetallic FeM@ZSM-5 (M=Ga, Ce, and Sn) was synthesized by mixing the sodium aluminate solution at a molar ratio of $Al_2O_3/SiO_2/TPAOH/Na_2O/H_2O$=1/180/36/5/4280. For more details, 0.06 g of $NaAlO_2$, 14.01 g of 1 M aqueous TPAOH, 0.13 g of NaOH, 4.67 g of FeM-SiO_2, and 18.68 g of water were thoroughly mixed and stirred at room temperature for 5 h. Then, the mixture was placed in a Teflon tube-installed autoclave for hydrothermal synthesis at 180 °C for 48 h. Finally, as-synthesized white powder was recovered by filtering and washing with deionized water several times, and all samples were dried at 180 °C for 48 h and calcined at 550 °C for 5 h. The as-prepared hierarchically-structured bimetallic catalysts were denoted as FeM@Z, where M stands for Ga, Ce, and Sn promoter and Z stands for ZSM-5 having a Si/Al molar ratio of 90. The reference FeCe/Z catalyst was prepared by using wet impregnation method by using same metal precursors at the fixed Fe and Ce contents with 10 and 1.5 wt%, respectively.

The catalytic cracking and reduction-oxidation activity of the fresh FeM@Z was measured in a stainless steel fixed-bed tubular reactor (inner diameter of 7 mm) at atmospheric pressure. For C_2H_6 dehydrogenation (reduction step by an initial oxidative dehydrogenation and steady-state catalytic cracking), the catalytic activity was measured with 20 vol% C_2H_6 balanced with N_2 at a space time (catalyst weight/volume flow rate, W/F)=0.4 (g·sec)/cm^3 at 600 °C for ~4 h. After the reduction step, N_2 was fed at the same temperature to purge out the residual gases without exposing it to air environment, and the CO_2 activation to CO (oxidation step) was subsequently performed at a higher temperature of 700 °C for ~2 h with 20 vol% CO_2 balanced with N_2. The products from the exit of reactor were monitored by using an online gas chromatograph (GC, YoungLin 6500) connected to a flame ionization detector (FID) with an HP-PLOT/Q capillary column to analyze hydrocarbons formed, as well as a thermal conductivity detector (TCD) with a Carboxen 1000 packed column to measure C_2H_6, C_2H_4, CH_4, CO, CO_2, and H_2. The intrinsic catalytic activity of turnover frequency (TOF (h^{-1})) was calculated by using the equation of [conversion (C_2H_6) x inlet moles of C_2H_6]/[CO uptake (mol/g_{cat}) x catalyst weight (g_{cat})]) and conversion of C_2H_6 and product distributions were calculated by using the following equations.

$$C_2H_6 \text{ conversion } (\%) = \frac{\text{moles of } C_2H_6^{in} - \text{moles of } C_2H_6^{out}}{\text{moles of } C_2H_6^{in}} \times 100$$

$$\text{Product distribution } (\%) = \frac{\text{moles of specific product}^{out}}{\text{moles of } C_2H_6^{in} - \text{moles of } C_2H_6^{out}} \times 100$$

2. Catalyst Characterization

Powder X-ray diffraction (XRD) patterns of the fresh FeM@Z were recorded on an X'Pert PRO MPD instrument by using a Cu-Kα radiation (λ=0.15418 nm) as an X-ray source in the 2θ range of 5-50°. The specific surface area (Sg, m^2/g) of the fresh FeM@Z was determined by using a Tristar II (Micromeritics) apparatus with Brunauer-Emmett-Teller (BET) method after degassing the sample in a vacuum condition at 350 °C for 3 h. X-ray photoelectron spectroscopy (XPS) was by using a VG Multilab 2000 instrument and the XPS spectra were recorded by using a Mg Kα X-ray source operating at 50 eV. Binding energy (BEs) of the XPS peaks was further corrected by using the reference BE of C 1s (284.6 eV). The outermost surface morphology of the FeM@Z was characterized by using field emission scanning electron microscopy (FE-SEM, JSM 6701f) operating at an accelerated voltage of 5 kV. The surface area of metallic Fe nanoparticles on the FeM@Z was measured by using CO chemisorption with an ASAP 2020 chemisorption analyzer (Micrometric). For more details, ~0.2 g of the fresh FeM@Z catalyst was pretreated under a vacuum condition at 350 °C for 4 h followed by reduction treatment at 600 °C for 4 h under an H_2 flow and degassed for 4 h. Thermal gravimetric analysis (TGA, TG50) was applied to verify the content of carbon formation by measuring it up to 1,000 °C under air environment.

The surface property of the FeM@Z was analyzed by temperature-programmed reduction with H_2 (H_2-TPR) analysis to measure the reduction behavior of metal oxides, and the surface cokes were measured by temperature-programmed surface reaction with H_2 (H_2-TPSR) to elucidate the coke precursors and content deposited after reduction-oxidation. In addition, temperature-programmed desorption of O_2 (O_2-TPD) was carried out to measure the oxygen vacant sites on the fresh FeM@Z with a BETCAT-M (Bel Japan) instrument equipped with TCD analyzer as well as connected to mass spectrometer, separately. Prior to H_2-TPR analysis, the fresh FeM@Z sample with 0.03 g was pretreated under a flow of Ar at 500 °C for 1 h to eliminate the adsorbed water and impurities and then cooled to 50 °C. After purging it with Ar, 10 vol%H_2/Ar gas was introduced to the sample cell and TPR patterns were obtained up to 1,000 °C at a ramping rate of 10 °C/min. The amount of coke precursors deposited on the used FeM@Z after reduction-oxidation cycles was measured by H_2-TPSR analysis through the

Table 1. Bulk and surface properties of the fresh bimetallic FeM@ZSM-5 (Me=Ce, Ga and Sn) catalysts

Catalyst	N_2-sorption[a]	XRF			XRD[b]	NH_3-TPD	H_2-TPR[c]	XPS (eV)[d]		Chemisorption[e]		
	S_g (m^2/g)	Fe (wt%)	M (wt%)	Molar ratio of Si/Al	Crystallinity (%) (fresh/reduced/ oxidized)	Acidity (mmol/g)	H_2 uptake (mmol/g_{cat}) (fresh/reduced/ oxidized)	BE of Fe $2p_{3/2}$	I_{Fe}/I_{si}	CO uptake (μmol/g_{cat})	D (%)	O_2 uptake (μmol/g_{cat})
Fe@Z	265.3	11.9	-	99.1	100.0/115.4/70.9	0.582	1.28/1.13/1.14	712.1	0.07	16	4.3	38
FeCe@Z	263.2	9.2	1.5	91.5	100.7/105.7/59.2	0.588	1.19/1.03/1.08	711.8	0.05	37	12.0	70
FeGa@Z	330.5	8.5	0.8	95.3	115.9/125.1/56.3	0.548	1.35/1.29/0.95	711.5	0.04	27	24.4	59
FeSn@Z	344.5	11.4	1.4	101.6	128.9/129.5/58.5	0.577	1.19/1.03/1.20	711.0	0.10	17	26.2	42

[a]S_g represents the specific surface area (m^2/g) measured by N_2 adsorption-desorption analysis.
[b]Crystallinity of the FeMe@ZSM-5 (Me=Ce, Ga and Sn) was calculated by comparing an integrated area of the most intense peak correspond to (011) and (200) based on the 100% of the fresh Fe@ZSM-5.
[c]Hydrogen uptake on the fresh, reduced by C_2H_6 dehydrogenation and oxidized bimetallic iron based ZSM-5 by CO_2 activation were calculated by using total consumed amount of hydrogen during TPR experiment.
[d]Binding energy (BE) of Fe $2p_{3/2}$ and intensity ratio of Fe to Si (denoted as I_{Fe}/I_{si}) on the fresh bimetallic iron based ZSM-5 were calculated by using the integrated and deconvoluted areas of the Fe $2p_{3/2}$ peak from XPS analysis.
[e]CO chemisorption was performed on the reduced FeMe@ZSM-5 by using a Micromeritics ASAP 2020C instrument after the reduction of FeMe@ZSM-5 under H_2 flow at 600 °C for 2 h and subsequent CO adsorption at 35 °C. The CO uptakes (μmol/g_{cat}) and dispersion (D, %) of the metallic Fe species on the catalyst were further calculated with a CO/Fe stoichiometry ratio of 0.5. The dispersion of Fe species was corrected by considering the degree of reduction (D_R) obtained from an O_2 titration and the O_2 uptake on the reduced Fe/TiO_2 was calculated under the same chemisorption conditions using the O_2 oxidant instead of CO molecule.

same procedures as described by H_2-TPR experiment with TCD analyzer. In addition, CH_4 and C_2H_6 species formed by H_2-TPSR were analyzed by measuring their separate fragments assigned to m/z=15 and 28 by using a quadrupole mass spectrometer (QMS 200 M2). O_2-TPD analysis was also carried out by using a BET-CAT-M (Bel Japan) instrument with a TCD analyzer, which was to measure oxygen vacant sites after pretreatment at 600 °C for 1 h under a flow of 1 vol%O_2/He. After cooling to room temperature under an He flow to remove physisorbed surface oxygen, O_2-TPD was carried out up to 1,000 °C at a ramping rate of 10 °C/min and the effluent gases were analyzed by using a quadrupole mass spectrometer (QMS200 M2) as well. Temperature-programmed desorption of methanol (CH_3OH-TPD) involved using a gas chromatograph as well as mass spectrometer (GC/MS) to determine the adsorption characteristics of methanol on the active sites of the FeM@Z. For the CH_3OH-TPD analysis, 0.1 g of sample was pretreated under a flow of 1 vol% O_2/He at 700 °C for 0.5 h and cooled to room temperature. For the adsorption of methanol, it was fed to the reactor under an He flow through a liquid pump for 1 h with a liquid methanol flow rate 0.02 ml/min, and the temperature was kept under a flow of pure He at 100 °C for 2 h to remove the physically adsorbed methanol molecules. All effluent components during CH_3OH-TPD were monitored by using a gas chromatograph as well as mass spectrometry (GC/MS, Yonglin 6900) by increasing the temperature to 700 °C at a ramping rate of 10 °C/min.

RESULTS AND DISCUSSION

1. Bulk and Surface Properties of FeM@ZSM-5 Catalysts

N_2 adsorption-desorption isotherms of the fresh FeM@Z (supplementary Fig. S1) revealed the formation of micropores with type I isotherm based on its obvious uptake at low pressure (P/P_0< 0.01). On the FeM/Z, the specific surface areas were found to be 263.2-344.5 m^2/g with its largest area of 344.5 m^2/g on the FeSn@Z and smallest one of 263.2 m^2/g on the FeCe@Z as summarized in Table 1. Compared with the hierarchically-structured spherical morphology of the Fe@Z with larger aggregated particles composed of smaller cubic plates (typical morphology of MFI-type ZSM-5) [18], the smaller ZSM-5 plate sizes with the typical cubic ZSM-5 structures in the much smaller spherical granules on the FeGa@Z and FeSn@Z were mainly responsible for the increased surface areas by generating dominant inter-particular mesopores. As shown in Fig. 1(A), 1(B) and supplementary Fig. S2, the spherical granule sizes of the fresh FeM@Z were found to be 2-4 μm with their different submicron-sized ZSM-5 plates (200-500×500-1,000 nm), where the smaller stacked ZSM-5 plates were observed on the FeGa@Z, FeCe@Z and pristine Fe@Z and larger ones on the FeSn@Z by the possible recrystallization of nano-crystallites to form the plate-like ZSM-5polycrystallites [19] with the help of small amount of Ga or Ce oxides (Fig. S2). Those different plate sizes of ZSM-5 on the spherical FeM@Z particles appear to be responsible for different specific surface areas, which were affected by the preparation step of Fe(M)-SiO_2 composites. It could be also attributed by their different ionic radius of the metal ions compared to those of Si and Al atoms, for example, similar ironic radius between Al and Ga atoms compared to that of Al and Ce or Sn atoms [20]. The XRD patterns of the FeM@Z with different metal oxides promoters are displayed in Fig. 2(c) and all catalysts show the typical MFI structure with their higher crystallinity by showing the intense characteristic diffraction peaks for the ZSM-5 facets such as the larger (101), (020), and (501) plane peak intensity [21]. However, the diffraction peaks for metal oxides such as Fe oxides are not

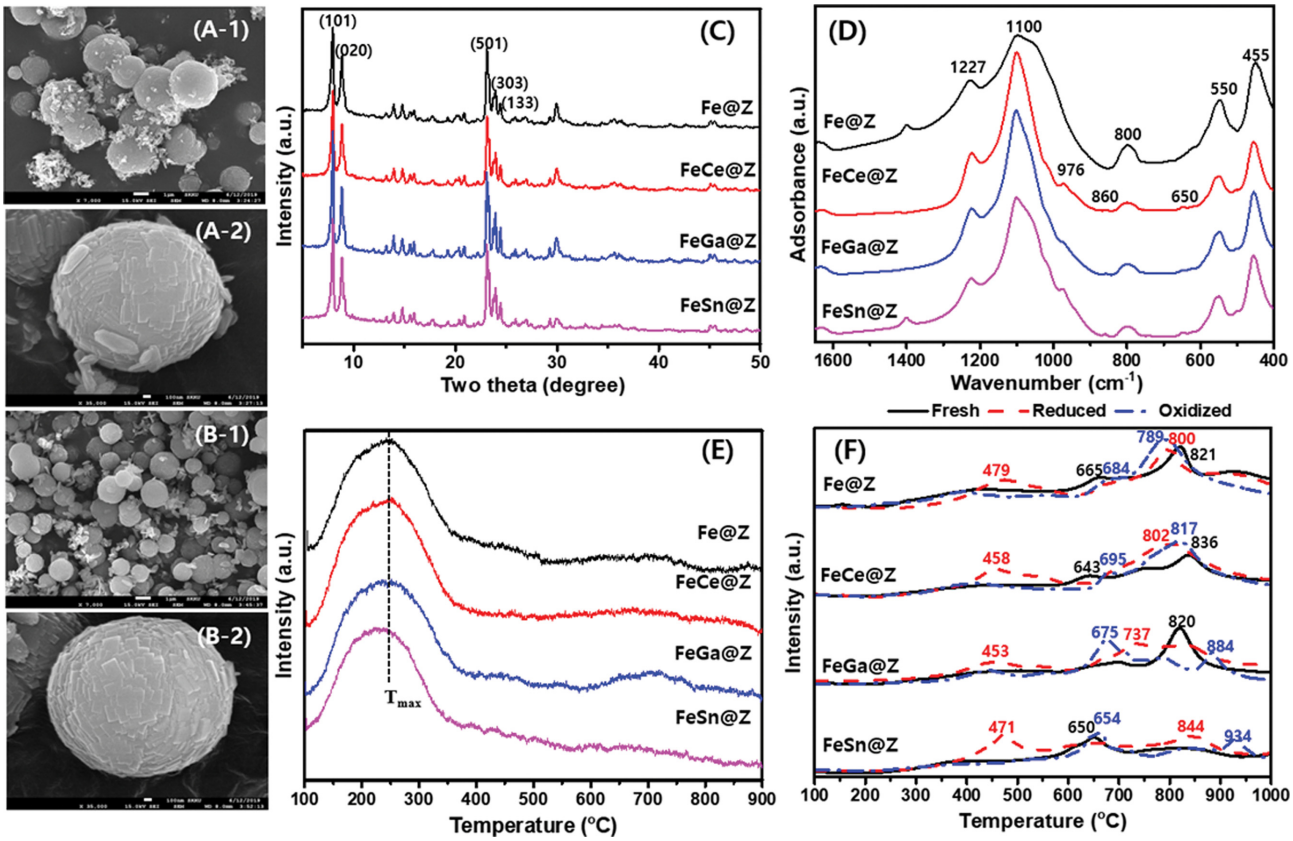

Fig. 1. Bulk and surface properties of the fresh bimetallic FeM@Z (M=Ce, Ga, and Sn) catalysts; (A) SEM image of Fe@Z and (B) SEM image of FeCe@Z with (1) larger scale of particles and (2) its magnified images, (C) XRD patterns, (D) FT-IR spectra, (E) NH_3-TPD profiles, (F) H_2-TPR profiles of the fresh (solid line with black color), reduced (after C_2H_6 conversion with dashed line with red color) and oxidized (after CO_2 activation with short dash dot line with blue color) catalysts.

clearly observed due to their amorphous nature or smaller content (concentration of M=0.8-1.5 wt% and that of Fe=8.5-11.9 wt%). The observations were also attributed to the possible interstitial substitutions of metal ions into the ZSM-5 framework with its different amounts. For example, the different Fe content of the respective values of 8.5 and 9.2 wt% on the FeGa@Z and FeCe@Z and the relatively smaller Si/Al ratios on the FeCe@Z and FeGa@Z in the range of 91.5-95.3 compared to that of 101.6 on the FeSn@Z also suggest the partial substitutions of the Si or Al sites of the ZSM-5 frameworks by second metals such as Ce and Ga atoms with their different dispersion and content. As summarized in Table 1, the relative crystallinity of the fresh FeM@Z (based on the 100% on the Fe@Z) was calculated by comparing the peak intensities appearing at 2θ=7.97 and 8.83°, and much lower relative crystallinity on the FeCe@Z with 100.7% was observed compared to the FeGa@Z and FeSn@Z with the respective values of 115.9 and 128.9%. The differences of the crystallinity on the fresh FeM@Z suggest that the promoters such as Ga and Sn metals on the FeM-SiO_2 composites are formed with its larger sizes on the ZSM-5 surfaces compared to that of Ce metal, where those Ga and Sn metal oxides play important roles as oxygen vacant sites by simultaneously altering the crystallinity as well as dispersion of iron oxides with their smaller substitution nature into the ZSM-5 frameworks. Therefore, the observed relatively lower crystallinity on the FeCe@Z (Fig. 1(C)) compared to other FeM@Z could be attributed to its possible substitution into ZSM-5 frameworks and the selective formation of newly formed intra-particular larger pores originating from the stacking of smaller aggregated plate-like ZSM-5 particles as confirmed by SEM images in Fig. 1 and supplementary Fig. S2.

The FT-IR analysis was carried out on the fresh FeM@Z (Fig. 1(D)), and the absorption peaks in the range of 400-1,600 cm^{-1} revealed the characteristic peaks of the skeleton vibrations of ZSM-5 frameworks with an insignificant contribution of the incorporated Fe and metal oxide promoters. In general, the absorption bands at ~1,100 and 455 cm^{-1} are attributed to the internal asymmetric stretching vibration modes of tetrahedral Al and Si sites, and the bands at ~1,227 and 550 cm^{-1} are assigned to the vibration modes of 5-membered ring (5-MR) channels in the Pentasil framework [22]. The characteristic absorption bands at 1,400 and 3,150 cm^{-1} as displayed in supplementary Fig. S3 were assigned to the N-H groups originating from residual ammonium ions, and the absorption band at ~800 cm^{-1} was induced from the external symmetric stretching mode of Si-O-Si structures as well as those at ~650, 860 and 976 cm^{-1} for the asymmetric stretching vibration modes of Si-O-T sites, where T is for other substituted metals. Therefore, the relatively larger peak intensities of the peaks at ~650 and 976 cm^{-1} with smaller one at ~800 cm^{-1} on the FeCe@Z compared to other FeM@Z suggest larger metal incorporation in the

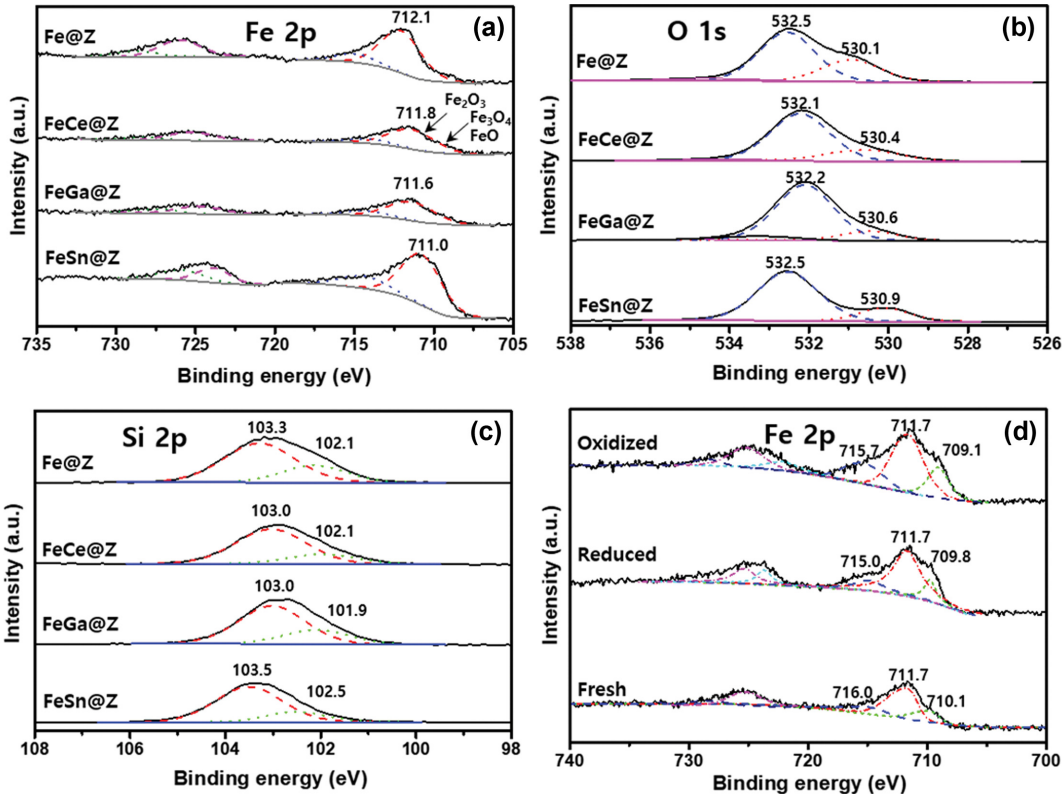

Fig. 2. XPS spectra of the fresh FeM@Z (M=Ce, Ga, and Sn) catalysts; (a) Fe 2p, (b) O 1s, (c) Si 2p, and (d) Fe 2p spectra of the fresh, reduced, and oxidized FeCe@Z.

ZSM-5 framework by causing higher local distortions and defects, which further leads to significantly different surface morphology of the FeM@Z. In addition, the similar peak intensity of weak absorption band at 3,667 cm^{-1} on all the FeM@Z suggests the existence of surface hydroxyl groups related to surface acidic sites originating from both silanol and bridging hydroxyl groups [23]. The bulk property of the FeM@Z seems to further change the surface property by altering the number of acidic sites and by changing the active oxygen vacant sites due to the incorporated metal ions or clusters as well.

Therefore, the surface acidic sites on the FeM@Z were measured by NH_3-TPD analysis and the desorption pattens are displayed in Fig. 1(E) and summarized in Table 1. On all FeM@Z, one broad desorption peak was observed with maximum desorption peak positions (T_{max}) at ~250 °C (assigned to weak acidic sites). The desorption peaks shifted to lower temperature on the bimetallic FeM@Z compared to the Fe@Z, especially on the FeSn@Z, which was attributed to the basic nature of SnO_2 nanoparticles with their preferential deposition on the outer surface in the form of $Sn(OH)_x$ species [24]. The amount of acidic sites on the FeM@Z was found to be in the range of 0.548-0.588 mmol/g with a maximum value of 0.588 mmol/g on the FeCe@Z. The strong acidic sites assigned to the desorption peak at ~700 °C were found to be larger on the Fe@Z and FeGa@Z compared to the FeCe@Z and FeSn@Z. This observation suggests the proper modification of the much stronger acidic sites with the Ce species, where the stronger acidic sites are generally responsible for coke deposition and fast catalyst deactivation [25]. The modified surface property of the hierarchically-structured ZSM-5 with the monometallic Fe or bimetallic Fe-Ce oxides is beneficial to obtain a higher activity through selective blockage of stronger acidic sites with enhanced metal dispersion.

2. Active Surface Oxygens on FeM@ZSM-5 Catalysts with their Redox Properties

The extent of surface and lattice oxygens with the redox properties and moderate acidity of the reducible metal oxides on zeolites is well related with oxidative dehydrogenation (ODH) and catalytic thermal cracking activity, mainly explained by Mars van Krevelen mechanism [26]. Therefore, the surface oxygens were measured by O_2-TPD analysis and the desorption patterns on the FeM@Z are displayed in supplementary Fig. S4. The desorption peaks appearing below 300 °C are ascribed to the chemically adsorbed oxygen species on the surface (assigned to α oxygen) and those peaks appearing above 800 °C are attributed to the oxygen species in the lattices (γ oxygen) of metal oxides [27]. The α-oxygens desorbed at 200-400 °C, which can be originating from excess non-stoichiometrically adsorbed electrophilic oxygens on the metal oxides or zeolite surfaces, are generally responsible for the preferential CO_x formation by the possible deep oxidation of C_2H_6 [28]. Interestingly, the introduction of Ce oxides induced the increase of the electrophilic surface O^- species due to the presence of cationic vacant sites [28], which resulted in increasing CO selectivity with 7.1% and suppressing deep ethane oxidation to CO_2 with its selectivity of 0.4% over the FeCe@Z. The peaks evolving at 800-950 °C

originated from the desorption of lattice oxygens on the metal oxides or zeolite surfaces, which are generally known to be active sites for the reduction-oxidation reactions assisted by the surface intermediates formed by the selective adsorption of reactants [28,29]. The desorbed amount of the lattice oxygens on the FeM@Z was found to be in the order of FeCe@Z>FeGa@Z>Fe@Z≈FeSn@Z as summarized in Table 1 and displayed in supplementary Fig. S4, which are well related with the conversion of C_2H_6. The larger oxygen vacant sites can be preferentially regenerated by redox cycles on the FeCe@Z by showing a lower C_2H_4 selectivity with slightly larger amount of CO on the active FeCe@Z and FeGa@Z. Based on the different reducibility of metal oxides on the FeM@Z, their crystallinity was increased after reduction step (C_2H_6 dehydrogenation) compared to the fresh FeM@Z in the range of 100.5-129.5% due to the reductive thermal treatment condition at 600 °C as summarized in Table 1. However, the crystallinity on the used FeM@Z was dramatically decreased after the oxidation step (CO_2 activation) at 700 °C in the range of 56.3-70.9 due to the possible degradation of the ZSM-5 structure by the phase transformation of metal oxides, which was found to be more significant on the FeGa@Z with the value of 56.3% and less impacted on the Fe@Z with 70.9%. Therefore, the adsorbed oxygen and its facile recovering nature of the lattice oxygen vacant sites of the metal oxides and comparable acidic sites, which acted as the active sites for catalytic cracking reaction during the present high temperature redox cycles, play the key roles for an enhanced C_2H_4 yield with much smaller coke deposition even under the structural disintegration conditions of the ZSM-5.

The reduction behavior of the fresh, reduced (after C_2H_4 dehydrogenation, reduction step) and oxidized (CO_2 activation, oxidation step) FeM@Z were measured by H_2-TPR analysis and the reduction patterns are displayed in Fig. 1(F) and summarized in Table 1. According to the previously reported results [29], three characteristic peaks are generally related to stepwise successive reduction of iron oxides such as the partial reduction of isolated and oligomeric clusters or nanoparticles from Fe^{3+} (Fe_2O_3) to surface Fe^{2+} (FeO) species below 500 °C [30], successive reduction of Fe^{2+} into metallic Fe^0 from the bulk phases of FeO or Fe_3O_4 at 500-750 °C and full reduction of isolated Fe^{2+} to metallic Fe^0 with the possible structural collapse of zeolites above 750 °C [31]. All H_2-TPR patterns on the fresh FeM@Z were found to be similar with their slightly different reduction peak intensity; however the FeSn@Z showed one larger broad reduction peak at ~650 °C and no other apparent peaks were observed at >750 °C. These observations possibly suggest the larger Fe-Sn bimetallic particles were preferentially formed on the external surface of the hierarchically-structured spherical ZSM-5 with their weaker interaction and smaller amount of the reducible oxygen vacant sites resulting in showing a lower catalytic activity. After the reduction step by C_2H_4 dehydrogenation on the FeM@Z, all iron oxides were partially reduced by showing new main reduction peaks at ~450 °C with the presence of much strongly interacting Fe nanoparticles on the ZSM-5 surfaces confirmed by the observed larger peaks at ~800 °C. Interestingly, the first reduction peaks after the reduction step were found to be much lower at 453-458 °C on the reduced FeCe@Z and FeGa@Z compared to those of the Fe@Z and FeSn@Z at 471-479 °C, which suggests more facile redox nature of the supported nanoparticles such as iron oxides and metal promoters on the FeCe@Z and FeGa@Z corresponding to an increased catalytic activity. After the oxidation step (CO_2 activation), the original reduction patterns were almost recovered on all the FeM@Z with little larger peak intensity at ~800 °C, except for the FeGa@Z due to its significant structural collapse of the ZSM-5 (lowest crystallinity of 56.3% as shown in supplementary Fig. S5 and Table 1) or heterogeneous size distribution of iron nanoparticles. In addition, total hydrogen consumption on the fresh, reduced and oxidized FeM@Z as summarized in Table 1 were slightly altered by showing invariant H_2 uptake in the range of 1.03-1.28 mmol/g, except for the FeGa@Z in the range of 0.95-1.35 mmol/g with their gradual decreasing patterns during reduction-oxidation steps. Therefore, the stable preservation of the reducible Fe and Ce nanoparticles on the FeCe@Z seems to be responsible for an increased catalytic activity by preserving active oxygen vacant sites with less structural disintegration of the ZSM-5 with the help of second metal promoter of CeO_2. To further verify the surface acidity and redox nature of the FeM@Z, methanol-TPD analysis was performed with a mass spectrometer to analyze the products [5,32] such as CO_2 (m/z=44), dimethyl ether (m/z=46), and formaldehyde (m/z=29), and the TPD patterns are shown in supplementary Fig. S6. The desorption peaks at ~200 and ~350 °C were assigned to formaldehyde (CH_2O) species, which was mainly attributed to methanol adsorption and its subsequent dehydration to dimethyl ether on the acidic sites selectively. The desorption peak at ~350 °C shifted to lower temperature regions on the FeCe@Z and FeGa@Z compared to that of the Fe@Z, and the fully oxidized CO_2 peak was also observed on the FeCe@Z and FeGa@Z, which have large amounts of surface oxygens due to the dispersed iron nanoparticles as well as acidic sites as confirmed by O_2-TPD analysis. The results of methanol-TPD revealed the significant change of acidic sites on the ZSM-5 surfaces during the incorporation of iron oxides and promoters, and the variations were found to be insignificant on the FeCe@Z by showing the clear desorption peaks of dimethyl ether on the acidic sites (Fig. S6 and Table 1).

The oxidation state and surface chemical composition on the FeM@Z are displayed in Fig. 2 and supplementary Fig. S7. The deconvoluted Fe 2p spectra can be assigned to the iron oxides of Fe^{2+} (BE=~708 eV), Fe^{3+} (BE=~711 eV) and Fe hydroxide (BE=~712 eV). The BEs of Fe 2p on the fresh FeM@Z were shifted from 712.1 eV on the Fe@Z to 711.0-711.8 eV on the bimetallic FeM@Z (Table 1), which strongly suggests the decreased oxidation state of Fe nanoparticles [33] due to the possible contribution of second metals through partial reduction of Fe nanoparticles by forming relatively larger sizes during the calcination and hydrothermal synthesis step. The copresence of Fe^{3+} and Fe^{2+} species such as Fe_2O_3 (or FeOOH) and Fe_3O_4 (or FeO) phases assigned to the BEs of 711-712 eV on the fresh FeM@Z suggests the redox properties of the iron oxides, where the lower BEs of the Fe 2p assigned to the partially reduced Fe^{2+} species were more obvious on the FeCe@Z and FeGa@Z compared to the Fe@Z (Fig. 2(a)). However, the fully oxidized Fe_2O_3 phases seem to be dominant on the FeSn@ZSM-5 as supported by one broad peak with a spin-coupled doublet for Fe $2p_{3/2}$ and Fe$2p_{1/2}$ at BEs of 711 and 724 eV, respectively [34]. As summarized in Table 1, the outermost sur-

face ratio of I_{Fe}/I_{Si} was found to be smaller on the FeCe@Z and FeGa@Z with 0.04-0.05 compared to the Fe@Z and FeSn@Z with 0.07-0.10, which also suggests the more homogeneous distribution of Fe nanoparticles on the active FeCe@Z and the larger aggregated particles were possibly formed in the order of FeCe@Z≤ FeGa@Z<Fe@Z<FeSn@Z. As shown in Fig. 2(b), the BEs of O 1s at 532.1-532.5 eV on the fresh FeM@Z also revealed the surface oxygen species assigned to the electrophilic O^{2-}, O_2^{2-}, or O^- species and those at 530.1-530.6 eV were assigned to the lattice oxygen species. In general, the higher ratio of the adsorbed surface oxygens to lattice oxygens on the FeM@Z seems to be responsible for the deeper oxidation of ethane to CO_x product, which was much smaller on the bimetallic FeM@Z (smaller deconvoluted peak intensity) compared to the Fe@Z. In addition, the slightly higher BEs of Fe 2p and O 1s on the Fe@Z were responsible for its lower catalytic activity due to the stronger interactions of Fe-O bonds on the ZSM-5 surfaces. These observations were found to be similar with Si 2p spectra (Fig. 2(c)). On the most active FeCe@Z, the BE of Fe $2p_{3/2}$ at 710.1 eV assigned to Fe^{2+} phases was decreased to 709.8 eV after C_2H_6 dehydrogenation (reduction) and the outermost surface Fe oxidation states were further reduced after CO_2 activation by showing its lower BE at 709.1 eV (Fig. 2(d)). However, the robust preservation of bulk Fe_2O_3 phases was observed on the FeCe@Z as supported by the observed same BEs of 711.7 eV during reduction-oxidation steps. High-resolution XPS spectra of Ce 3d (supplementary Fig. S7(a)) also suggest the presence of mixed oxidation states of Ce species (Ce^{3+}/Ce^{4+}) [35] on the reduced and oxidized FeCe@Z, and the ratio of Ce^{3+}/Ce^{4+} was found to be ~0.54, which also indicates the facile redox nature of Ce oxides between Ce^{3+} and Ce^{4+} phases during reduction-oxidation cycles. The Ga $2p_{3/2}$ spectra on the FeGa@Z are displayed in Fig. S7(b) at reduction-oxidation steps. The BE of Ga $2p_{3/2}$ on the FeGa@Z was found to be ~1,117.9 eV, assigned to the Ga^{3+} species such as Ga_2O_3 phase [36], which were not largely altered during the reduction-oxidation steps due to its irreducible nature. In addition, the Sn 3d spectra on the FeSn@Z as displayed in Fig. S7(c) are assigned to the Sn^{4+} species with SnO_2 phase, and the BEs of the Sn 3d were not varied significantly according to reduction-oxidation steps due to its stronger interaction on the ZSM-5 surface. Those different oxidation states of the promoters on the FeM@Z during reduction-oxidation steps can alter the catalytic activity, and Ce oxides seem to be proper by possessing a facile reduction-oxidation nature with their proper Ce^{3+}/Ce^{4+} ratios. Those active oxygen vacant sites acting as an active sites for catalytic cracking reaction were further measured by CO and O_2 chemisorption by using the fresh FeM@Z (Table 1), and the larger CO uptake with 37 μmol/g and larger O_2 uptake with 70 μmol/g were observed on the FeCe@Z with the higher metal dispersion of active iron nanoparticles as well as promoter (12%) compared to other FeM@Z (For example, CO uptake with 16 μmol/g and O_2 uptake with 38 μmol/g with dispersion of 4.3%. on the Fe@Z). Those findings suggest the preferential formation of the smaller Fe nanoparticles on the stable acidic FeCe@Z surface via a partial substitution of Fe and Ce metal ions into ZSM-5 framework. The Fe nanoparticles on the FeCe@Z also revealed the higher redox property between Fe^{3+} and Fe^{2+} phases with the help of the reducible Ce oxides [28], which was found to be similar on the FeGa@Z by showing a larger O_2 uptake (59 μmol/g). However, the observed smaller CO and O_2 uptake on the Fe@Z and FeSn@Z was attributed to the strongly interacting larger Fe nanoparticles aggregated on the outer surface of the hierarchically-structured spherical ZSM-5.

3. Catalytic Activity for Reduction-oxidation Reaction and Resistance to Coke Formation

The catalytic activity and product distribution on the FeM@Z were successively measured by C_2H_6 dehydrogenation (reduction step including catalytic thermal cracking) and subsequent CO_2 activation (oxidation step) and the results are summarized in Table 2 and displayed in Fig. 3. The higher conversion of C_2H_6 (6.1%) and lower selectivity to C_2H_4 (89.8%) were observed on the FeCe@Z with a little higher CO_x selectivity (~7.4%) due to an excess amount

Table 2. Catalytic activity and product distribution for C_2H_6 dehydrogenation and subsequent CO_2 activation on the bimetallic FeM@ZSM-5 (Me=Ce, Ga and Sn) catalysts

Catalyst	C_2H_6 dehydrogenation[a]				CO_2 activation[b]
	TOF (h^{-1})	C_2H_6 conv. (%)	Product distribution ($CO/CO_2/CH_4/C_2H_4$)	C_2H_4 yield (%)	CO formed ($mmol/g_{cat}$)
Fe@Z	20	0.7	0.4/1.0/1.1/97.5	0.7	1.9
FeCe@Z	83	6.1	7.0/0.4/2.8/89.8	5.5	9.7
FeGa@Z	59	3.2	2.3/0.9/8.2/88.6	2.8	7.9
FeSn@Z	57	2.0	0.6/1.3/7.2/90.9	1.8	2.3
FeCe/Z	57	4.3	0.5/2.1/4.2/93.2	4.0	5.9

[a]C_2H_6 dehydrogenation (conversion of C_2H_6, X, mol%) was carried out on the fresh Fe@ZSM-5 and pristine Fe@ZSM-5 for its reduction reaction at the reaction conditions of T=600 °C, P=0.1 MPa, space time (catalyst weight/volume flow rate, W/F)=0.4 (g·sec)/cm^3 by using a feed gas ratio of C_2H_6/N_2=0.25. Turnover frequency (TOF, h^{-1}) was obtained based on the conversion of C_2H_6 dehydrogenation with the measured surface area of Fe nanoparticles on the fresh Fe@ZSM-5 and pristine Fe@ZSM-5 using the equation of (TOF (h^{-1})=[conversion (C_2H_6) x inlet moles of C_2H_6]/[CO uptake (mol/g_{cat}) x catalyst weight (g_{cat})]).

[b]CO_2 activation was carried out just after the reduction reaction by C_2H_6 dehydrogenation on the fresh Fe@ZSM-5 and pristine Fe@ZSM-5 after its previous purging treatment under N_2 flow at the reaction conditions of T=700 °C, P=0.1 MPa, space time (catalyst weight/volume flow rate, W/F)=0.4 (g·sec)/cm^3 by using a feed gas ratio of CO_2/N_2=0.25.

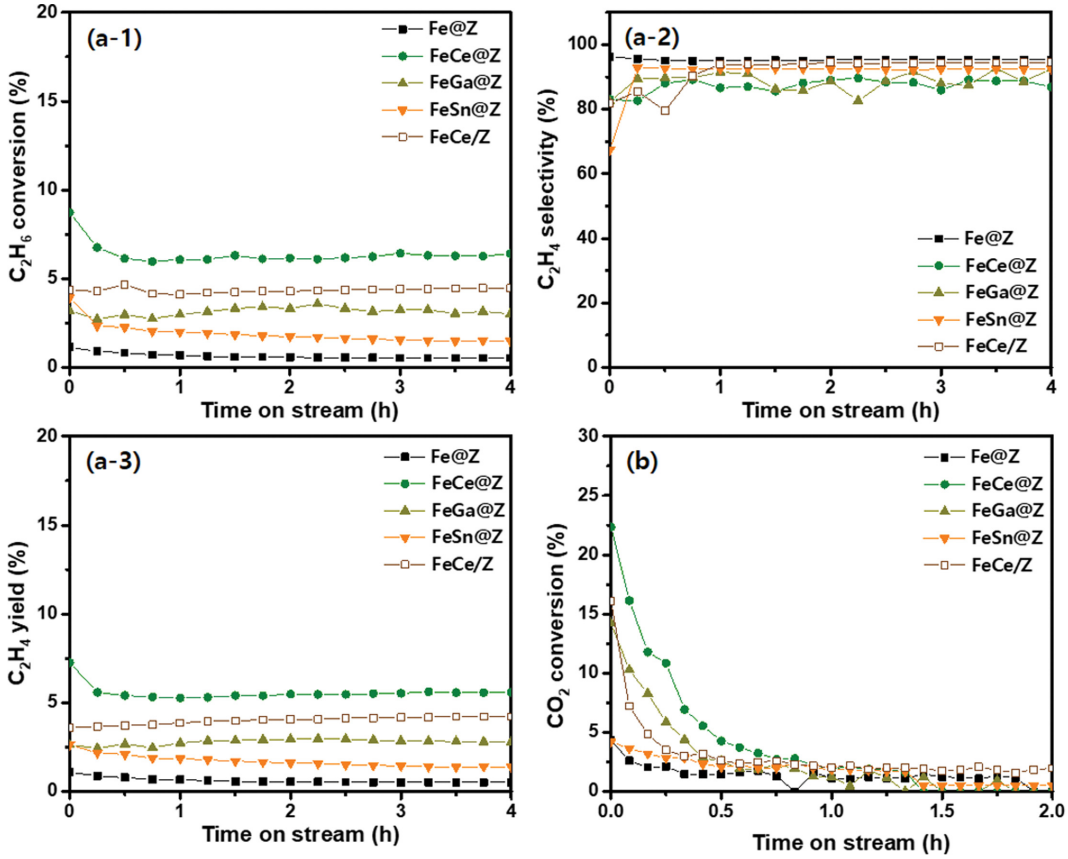

Fig. 3. Catalytic activity for the reduction-oxidation reaction on the bimetallic FeM@Z (M=Ce, Ga, and Sn) catalysts with the reference impregnated FeCe/Z catalyst at the reaction conditions for C_2H_6 dehydrogenation step (T=600 °C, W/F=0.4 (g·s)/cm^3 and C_2H_6/N_2 molar ratio=2/8) such as (a-1) C_2H_6 conversion, (a-2) C_2H_4 selectivity, (a-3) C_2H_4 yield with time on stream (h), and (b) CO_2 conversion at the reaction conditions for successive oxidation step (T=700 °C, W/F=2 (g·s)/cm^3 and CO_2/N_2 molar ratio=2/8).

of surface hydrophilic oxygens, which are comparable to a lower conversion of C_2H_6 of 0.7% with higher selectivity to C_2H_4 (97.5%) on the Fe@Z. Moderate conversion of C_2H_6 with 2.0-3.2% with higher selectivity to C_2H_4 with 88.6-90.9% was observed on the FeGa@Z and FeSn@Z. Therefore, the yield of C_2H_4 decreased in the order of FeCe@Z (5.5%)>FeGa@Z (2.8%)>FeSn@Z (1.8%)> Fe@Z (0.7%). On the bimetallic FeCe@Z, the higher yield of C_2H_4 was mainly attributed to larger active surface oxygen vacant sites and comparable acidic sites as well as its higher redox property with relatively homogeneous size distribution of the Fe nanoparticles compared to the monometallic Fe@Z. As shown in Fig. 3, stable conversion of C_2H_6 for ~4 h on stream (reduction step) was observed on the FeCe@Z through an initial oxidative dehydrogenation reaction of C_2H_6 ($C_2H_6+MO_x \rightarrow C_2H_4+MO_{x-1}+H_2O$) with its fast decreasing nature of C_2H_6 conversion and subsequent catalytic thermal cracking reaction of C_2H_6 with a relatively longer steady-state activity. This observation was confirmed by a mass spectrometer with the observation of water formation at an initial reaction period instead of hydrogen formed by thermal catalytic cracking reaction ($C_2H_6 \rightarrow C_2H_4+H_2$) on the acidic sites from our previous work [28]. However, C_2H_6 conversion slightly decreased from the very beginning of reaction for ~1 h on stream on the other FeM@Z due to the fast consumption of the smaller amount of active sites (oxygen vacant and acidic sites) and due to the possible surface coke deposition. By using CO chemisorption results (measurements of all oxygen vacant sites on the FeM@Z), turnover frequencies (TOF, h^{-1}) for C_2H_6 dehydrogenation on the FeM@Z are summarized in Table 2 and the intrinsic TOFs were found to be highest on the FeCe@Z with 83 h^{-1} and lowest on the Fe@Z and FeSn@Z with 20-57 h^{-1}. The FeCe@Z was found to be superior to Fe-impregnated reference FeCe/Z (TOF of 57 h^{-1}), which showed C_2H_6 conversion of 4.3% and C_2H_4 yield of 4.0% due to the less homogeneous distribution of the active Fe and Ce oxides possibly.

The surface nature of the most active FeCe@Z was mainly related to the redox property of oxygen vacant sites of the highly-dispersed metal oxides and comparable surface acidity for robust reduction-oxidation cycles as well as its stable catalytic cracking behavior. The incorporated and partially reducible Ce oxide promoter in the ZSM-5 structure can effectively increase O^{2-} diffusion to active Fe nanoparticles, which caused to increase C_2H_6 conversion as confirmed by O_2-TPD, chemisorption and XPS analysis. The reductions of iron oxides during reduction step with the help of Ce oxides having larger lattice oxygen mobility [35,37] can form active oxygen vacant sites even at lower temperature of 550 °C, which can be active sites for the subsequent CO_2 activation on the reduced FeCe@Z at a higher temperature of 700 °C. The dissociated CO_2 molecules

on the oxygen vacant sites can be converted to CO, and total amount of CO generated by CO_2 activation step was found to be in the range of 1.9-9.7 mmol/g with its highest value of 9.7 mmol/g on the most active FeCe@Z. Generally, the introduction of the partially reducible Ce or Ga metal oxides is capable of increasing oxygen vacant sites, which accelerate oxygen transfer rate into Fe nanoparticles [28,37]. In addition, the reverse Boudouard reaction [12a, 38] ($C+CO_2 \leftrightarrow 2CO$) of the surface cokes formed during dehydrogenation (reduction step) can also increase CO formation rate, which was responsible for the structural instability of the FeM@Z. We believe that the larger vacant sites with the help of Ce oxide promoter can enhance the rate of dehydrogenation reaction and CO formation. The longer production period of C_2H_4 formed by oxidative dehydrogenation of C_2H_6 as well as CO formed by successive CO_2 activation than those of the estimated stoichiometric amount of active oxygen sites on the FeM@Z was attributed to the contribution of thermal catalytic cracking reaction of C_2H_6 and reverse Boudouard reaction with surface carbons, respectively.

To respectively check the coke deposition on the used FeM@Z after C_2H_6 dehydrogenation and CO_2 activation, H_2-TPSR experiment by using a mass spectrometer and TGA analysis was carried out separately. H_2-TPSR patterns on the used FeM@Z just after C_2H_6 dehydrogenation (supplementary Fig. S8(a-1) and S8(b-1)) showed insignificant coke formation without showing any apparent CH_4 peak (m/z=15), which indicates the smaller coke formation even under the present harsh dehydrogenation condition at 600 °C due to the selective consumption of active surface oxygen species. In addition, TGA profiles on the used FeM@Z after C_2H_6 dehydrogenation also revealed smaller weight loss of ~3% below 200 °C only, which can originate from the desorption of surface hydroxy groups of the ZSM-5. The observations suggest smaller coke deposition owing to the usage of the surface and lattice oxygen species for an initial C_2H_6 dehydrogenation step and insignificant coke formation after CO_2 activation (supplementary Fig. S8(a-2) and S8(b-2)), The phenomena were attributed to the possible reoxidation of surface cokes by reverse Boudouard reaction as well as regeneration of oxygen vacant sites by CO_2 dissociation without forming iron carbides.

In summary, the bimetallic FeCe@Z with an insignificant coke formation during reduction step (dehydrogenation of C_2H_6) with its superior stability for a successive CO_2 activation to CO seems to be one of the alternative catalytic systems for the further application to chemical looping (CL) process as well as catalytic thermal cracking reaction. The CL-based successive C_2H_6 dehydrogenation and activation of CO_2 can prevent undesired CO_x formation by direct oxidative dehydrogenation of paraffins to olefins as well as to simultaneously activate CO_2 to value-added CO intermediate. The superior performance on the FeCe@Z was mainly attributed to its facile cyclic redox nature of the well-dispersed Fe nanoparticles with the help of the partially reduced CeO_2 and FeOx species as well as comparable amount of surface acidic sites, which were found to be active for a long-term catalytic cracking reaction as well.

CONCLUSIONS

The dehydrogenation of C_2H_6 to C_2H_4 and subsequent CO_2 activation to CO were investigated by reduction-oxidation reaction steps on hierarchically-structured bimetallic FeM@ZSM-5 (M=Ce, Ga and Sn), which can be possibly applied for conceptual design of chemical looping (CL) process through stable catalytic cracking of paraffins and successive oxidation of surface cokes. The higher redox nature of the well-dispersed Fe nanoparticles (partially reduced phases such as Fe_2O_3 and Fe_3O_4) with the help of second metal promoter such as the partially reducible CeO_2 on the hierarchically-structured acidic ZSM-5 surfaces was responsible for an enhanced catalytic activity (higher TOF value of 83 h^{-1} and CO_2 formation of 9.7 $mmol/g_{cat}$) without any coke formation. The enhanced catalytic activity on the FeCe@Z under the harsh reduction-oxidation steps was also largely affected by the acidic ZSM-5 surfaces through the preferential generation of larger amount of oxygen vacant sites. The superior activity and stability of the hierarchically-structured FeCe@Z were mainly attributed to the incorporated CeO_2 by stabilizing the oxidation states of Ce and Fe nanoparticles with their higher thermal stability of the FeCe@ZSM-5. The proper selection of second metal promoter (CeO_2) on the Fe@ZSM-5 seems to be a crucial factor to design the efficient redox catalytic system for C_2H_6 dehydrogenation with stable catalytic thermal cracking activity and subsequent CO_2 activation.

ACKNOWLEDGEMENTS

The authors would like to sincerely acknowledge the financial support from the National Research Foundation of Korea (NRF) grant funded by the Korea government (Project #: NRF- 2018M3 D3A1A01018009 and NRF-2020R1A2C2006052).

SUPPORTING INFORMATION

Additional information as noted in the text. This information is available via the Internet at http://www.springer.com/chemistry/journal/11814.

REFERENCES

1. (a) M. Dixit, P. Kostetskyy and G. Mpourmpakis, *ACS Catal.*, **8**, 11570 (2018); (b) Y. He, Y. Song and S. Laursen, *ACS Catal.*, **9**, 10464 (2019); (c) Y. Gao, L. Neal, D. Ding, W. Wu, C. Baroi, A. M. Gaffney and F. Li, *ACS Catal.*, **9**, 8592 (2019).
2. (a) S. Yusuf, V. Haribal, D. Jackson, L. Neal and F. Li, *Appl. Catal. B.*, **257**, 117885 (2019); (b) X. Li, A. Kant, Y. He, H. V. Thakkar, M. A. Atanga, F. Rezaei, D. K. Ludlow and A. A. Rownaghi, *Catal. Today*, **276**, 62 (2016).
3. (a) C. He and F. You, *Ind. Eng. Chem. Res.*, **53**, 11442 (2014); (b) M. Yang, X. Tian and F. You, *Ind. Eng. Chem. Res.*, **57**, 5980 (2018); (c) Z. J. Zhao, T. Wu, C. Xiong, G. Sun, R. Mu, L. Zeng and J. Gong, *Angew. Chem. Int. Ed.*, **57**, 6791 (2018).
4. (a) D. P. Solowey, M. V. Mane, T. Kurogi, P. J. Carroll, B. C. Manor, M.-H. Baik and D. J. Mindiola, *Nat. Chem.*, **9**, 1126 (2017); (b) H. Li, S. A. Kadam, A. Vimont, R. F. Wormsbecher and A. Travert, *ACS Catal.*, **6**, 4536 (2016).
5. S. Yusuf, L. Neal, Z. Bao, Z. Wu and F. Li, *ACS Catal.*, **9**, 3174 (2019).
6. V. P. Haribal, L. M. Neal and F. Li, *Energy*, **119**, 1024 (2017).

7. D. Lee, H. J. Ryu, D. Shun, D. H. Bae and J. I. Baek, *Korean J. Chem. Eng.*, **35**, 1257 (2018).
8. Y. S. Yun, M. Lee, J. Sung, D. Yun, T. Y. Kim, H. Park, K. R. Lee, C. K. Song, Y. Kim, J. Lee, Y.-J. Seo, I. K. Song and J. Yi, *Appl. Catal. B.*, **237**, 554 (2018).
9. Z. Skoufa, E. Heracleous and A. A. Lemonidou, *J. Catal.*, **322**, 118 (2015).
10. (a) M. D. Porosoff, M. N. Z. Myint, S. Kattel, Z. Xie, E. Gomez, P. Liu and J. G. Chen, *Angew. Chem. Int. Ed.*, **54**, 15501 (2015); (b) E. Gomez, X. Nie, J. H. Lee, Z. Xie and J. G. Chen, *J. Am. Chem, Soc.*, **141**, 17771 (2019).
11. (a) S. Yao, B. Yan, Z. Jiang, Z. Liu, Q. Wu, J. H. Lee and J. G. Chen, *ACS Catal.*, **8**, 5374 (2018); (b) E. Gomez, Z. Xie and J. G. Chen, *AIChE J.*, **65**, e16670 (2019).
12. (a) L. M. Neal, V. P. Haribal and F. Li, *Science*, **19**, 894 (2019); (b) L. M. Neal, S. Yusuf, J. A. Sofranko and F. Li, *Energy Technol.*, **4**, 1200 (2016).
13. L. C. Wang, Y. Zhang, J. Xu, W. Diao, S. Karakalos, B. Liu, X. Song, W. Wu, T. He and D. Ding, *Appl. Catal. B.*, **256**, 117816 (2019).
14. (a) M. W. Schreiber, C. P. Plaisance, M. Baumgärtl, K. Reuter, A. Jentys, R. Bermejo-Deval and J. A. Lercher, *J. Am. Chem, Soc.*, **140**, 4849 (2018); (b) A. Samanta, X. Bai, B. Robinson, H. Chen and J. Hu, *Ind. Eng. Chem. Res.*, **56**, 11006 (2017); (c) S. W. Choi, W.-G. Kim, J.-S. So, J. S. Moore, Y. Liu, R. S. Dixit, J. G. Pendergast, C. Sievers, D. S. Sholl, S. Nair and C. W. Jones, *J. Catal.*, **345**, 113 (2017).
15. E. A. Pidko, V. B. Kazansky, E. J. M. Hensen and R. A. van Santen, *J. Catal.*, **240**, 73 (2006).
16. J. H. Yun and R. F. Lobo, *J. Catal.*, **312**, 263 (2014).
17. Y. Zhang, Y. Zhou, A. Qiu, Y. Wang, Y. Xu and P. Wu, *Catal. Commun.*, **7**(11), 860 (2006).
18. H. Huang, H. Zhu, Q. Zhang and C. Li, *Korean J. Chem. Eng.*, **36**, 210 (2019).
19. X. Chen, M. Qiao, S. Xie, K. Fan, W. Zhou and H. He, *J. Am. Chem, Soc.*, **129**, 13305 (2007).
20. M. Saeidi and M. Hamidzadeh, *Res. Chem. Intermed.*, **43**, 2143 (2017).
21. R. Feng, X. Yan, X. Hu, Y. Zhang, J. Wu and Z. Yan, *Appl. Catal. A*, **594**, 117464 (2020).
22. R. M. Mohamed, H. M. Aly, M. F. El-Shahat and I. A. Ibrahim, *Micropor. Mesopor. Mater.*, **79**, 7 (2005).
23. L. G. A. van de Water, J. C. van der Waal, J. C. Jansen, M. Cadoni, L. Marchese and T. Maschmeyer, *J. Phys. Chem. B*, **107**, 10423 (2003).
24. X. Cui, Y. Zhu, Z. Hua, J. Feng, Z. Liu, L. Chen, J. Shi, *Energy Environ. Sci.*, **8**, 1261 (2015).
25. (a) Y. Zhang, M. Xue, Y. Zhou, H. Zhang, W. Wang, Q. Wang and X. Sheng, *RSC Adv.*, **6**, 29410 (2016); (b) S. Kasipandi and J. W. Bae, *Adv. Mater.*, **31**, 1803390 (2019)
26. Z. Sarshar, Z. Sun, D. Zhao and S. Kaliaguine, *Energy Fuels*, **26**, 3091 (2012).
27. J. Zhu, Z. Zhao, D. Xiao, J. Li, X. Yang and Y. Wu, *J. Mol. Catal. A*, **238**, 35 (2005).
28. M. H. Jeong, J. Sun, G. Y. Han, D. H. Lee and J. W. Bae, *Appl. Catal. B.*, **270**, 118887 (2020).
29. M. H. Jeong, D. H. Lee, G. Y. Han, C.-H. Shin, M. K. Shin, C. K. Ko and J. W. Bae, *Fuel*, **202**, 547 (2017).
30. E. Yuan, G. Wu, W. Dai, N. Guan and L. Li, *Catal. Sci. Technol.*, **7**, 3036 (2017).
31. Y. Lai and G. Veser, *Catal. Sci. Technol.*, **6**, 5440 (2016).
32. (a) T. Feng and J. M. Vohs, *J. Catal.*, **221**, 619 (2004); (b) C. L. Li and Y. C. Lin, *Appl. Catal. B.*, **107**, 284 (2011).
33. C. Wang, H. Shi and Y. Li, *Appl. Surf. Sci.*, **257**, 6873 (2011).
34. L. Freire, X. R. Nóvoa, M. F. Montemor and M. J. Carmezim, *Mater. Chem. Phys.*, **114**, 962 (2009).
35. K. Kuntaiah, P. Sudarsanam, B. M. Reddy and A. Vinu, *RSC Adv.*, **3**, 7953 (2013).
36. I. A. Hassan, S. Sathasivam, H. U. Islam, S. P. Nair and C. J. Carmalt, *RSC Adv.*, **7**, 551 (2017).
37. D. Chen, D. He, J. Lu, L. Zhong, F. Liu, J. Liu, J. Yu, G. Wan, S. He and Y. Luo, *Appl. Catal. B*, **218**, 249 (2017).
38. T. Lei, C. Miao, W. Hua, Y. Yue, Z. Gao, *Catal. Lett.*, **148**, 1634 (2018).

Supporting Information

Dehydrogenation of ethane and subsequent activation of CO_2 on hierarchically-structured bimetallic FeM@ZSM-5 (M=Ce, Ga, and Sn)

Min Hye Jeong[‡], Kyung Soo Park[‡], Dong Ming Shen[‡], Ji Won Moon, and Jong Wook Bae[†]

School of Chemical Engineering, Sungkyunkwan University (SKKU),
2066 Seobu-ro, Jangan-gu, Suwon, Gyeonggi-do 16419, Korea
(*Received 29 September 2020 • Revised 6 November 2020 • Accepted 7 November 2020*)

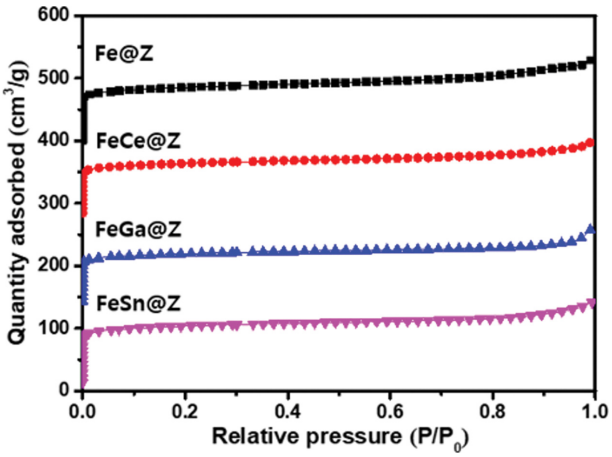

Fig. S1. N_2 adsorption-desorption isotherms of the fresh bimetallic FeM@Z (M=Ce, Ga, and Sn) catalysts.

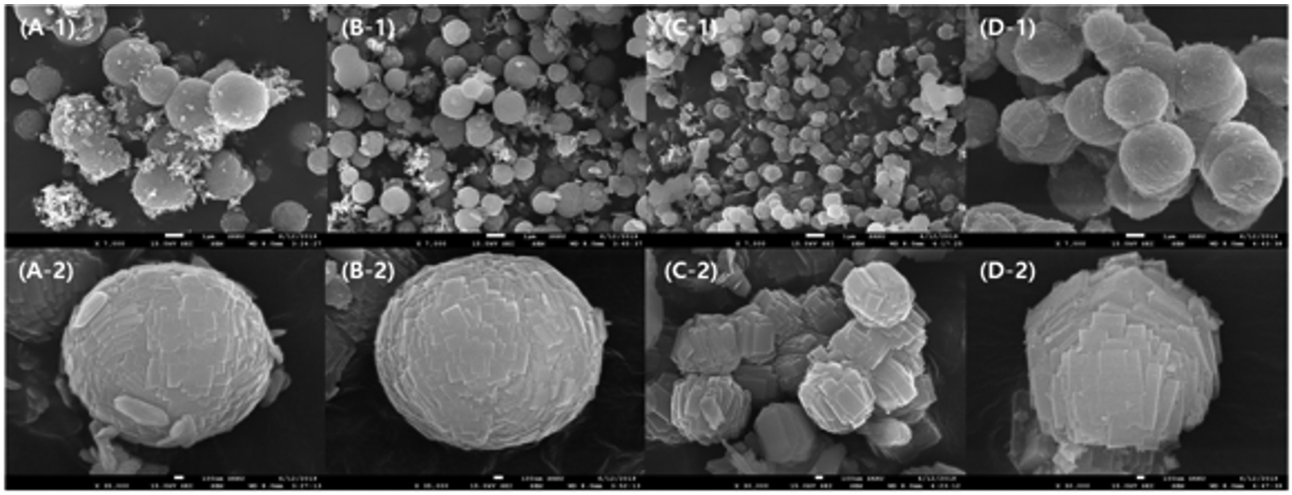

Fig. S2. Representative (field emission) SEM images of the fresh bimetallic (A-1) Fe@Z, (B-1) FeCe@Z, (C-1) FeGa@Z, and (D-1) FeSn@Z catalyst with their magnified images for the (A-2) Fe@Z, (B-2) FeCe@Z, (C-2) FeGa@Z, and (D-2) FeSn@Z catalyst.

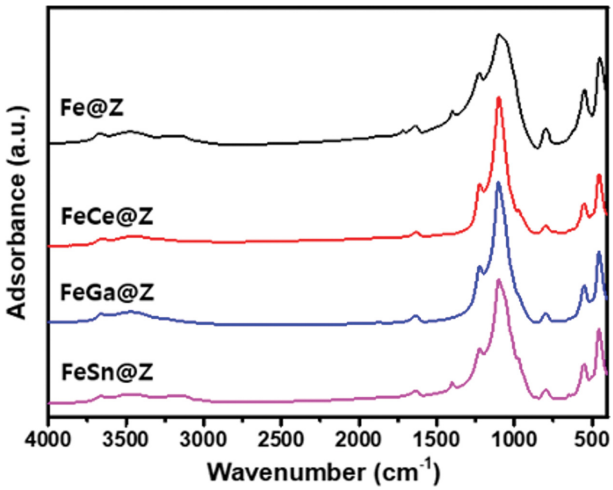

Fig. S3. Full range FT-IR spectra of the fresh bimetallic FeM@Z (M=Ce, Ga, and Sn) catalysts.

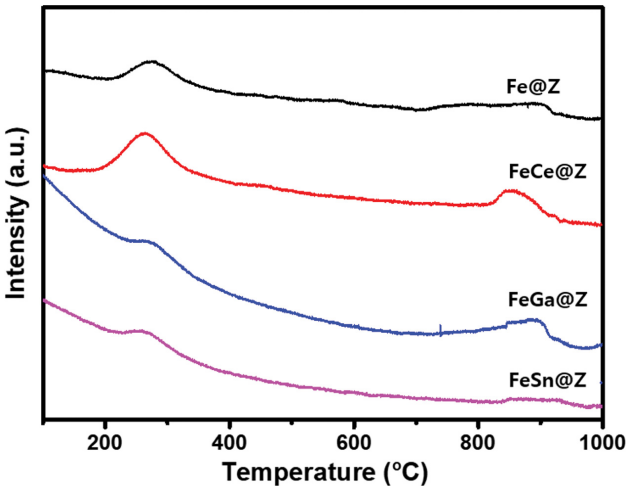

Fig. S4. O_2-TPD profiles of the fresh bimetallic FeM@Z (M=Ce, Ga, and Sn) catalysts.

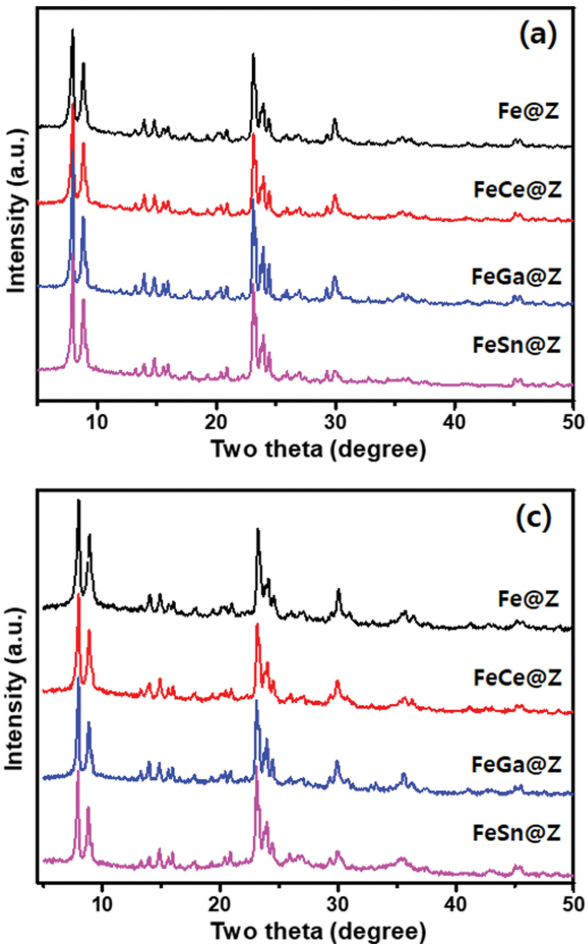

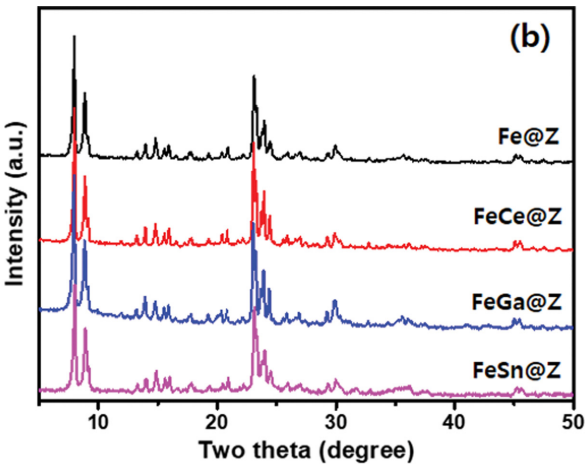

Catalyst	XRD Crystallinity (%) (fresh/reduced/oxidized)
Fe@Z	100.0/115.4/70.9
FeCe@Z	100.7/105.7/59.2
FeGa@Z	115.9/125.1/56.3
FeSn@Z	128.9/129.5/58.5

Fig. S5. XRD patterns of the bimetallic FeM@Z (M=Ce, Ga, and Sn) catalysts; (a) fresh FeM@Z, (b) reduced FeM@Z after C_2H_6 dehydrogenation (reduction step), (c) oxidized FeM@Z after subsequent CO_2 activation (oxidation step).

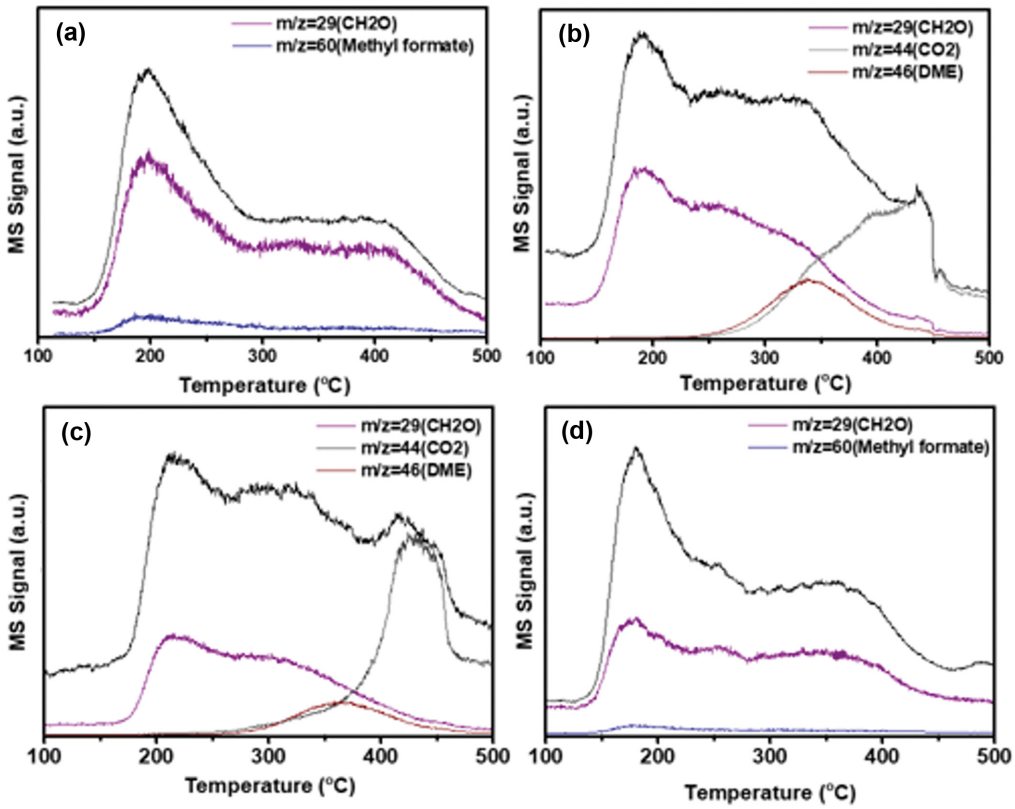

Fig. S6. Methanol-TPD profiles on the bimetallic FeM@Z catalysts; (a) Fe@Z, (b) FeCe@Z, (c) FeGa@Z, and (d) FeSn@Z.

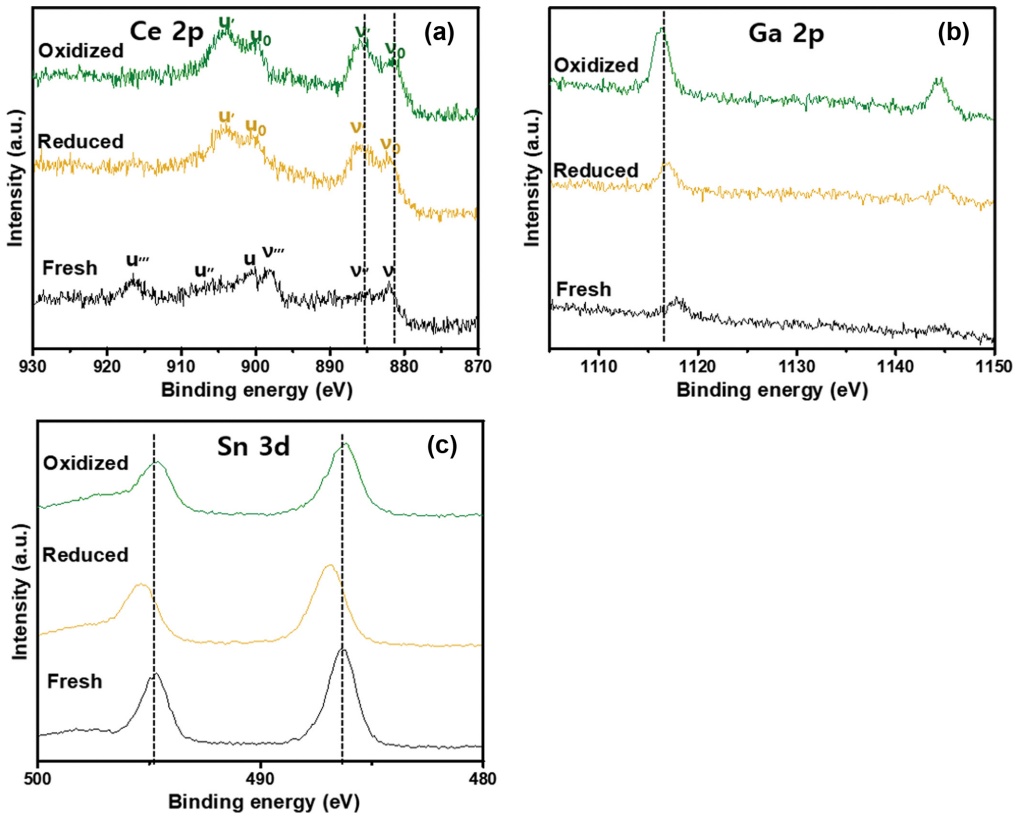

Fig. S7. XPS spectra of the fresh, reduced (after C_2H_6 dehydrogenation), and oxidized (after CO_2 activation) bimetallic FeM@Z catalysts; (a) Ce 2p on the FeCe@Z; (b) Ga 2p on the FeGa@Z; (c) Sn 3d on the FeSn@Z.

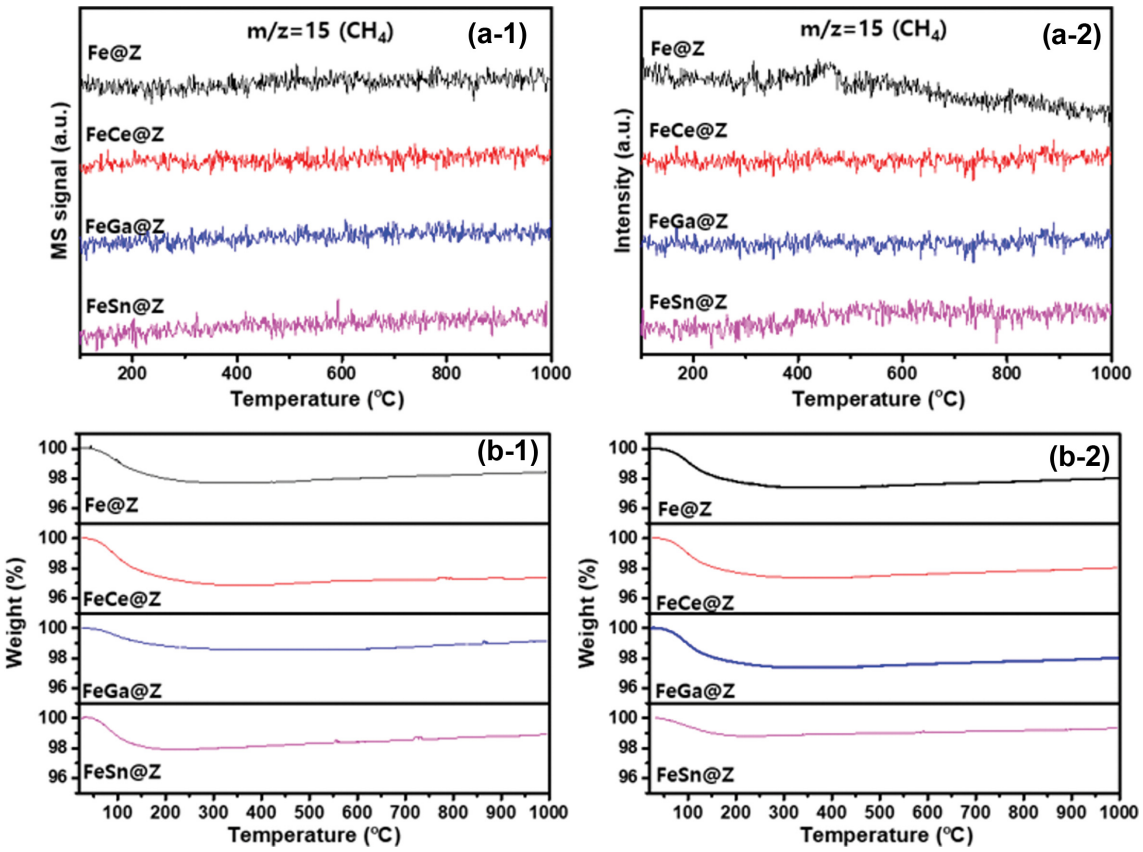

Fig. S8. TPSR profiles of the used FeM@Z (Me=Ce, Ga, and Sn) catalysts measured by GC-MASS (methane fragment assigned to m/z=15); (a-1) after C_2H_6 dehydrogenation step (reduction step) at the reaction conditions of T=600 °C, W/F=0.4 (g·s)/cm^3 and C_2H_6/N_2 molar ratio=2/8, (a-2) after CO_2 activation step (oxidation step) at the reaction conditions of T=700 °C, W/F=2 (g·s)/cm^3 and CO_2/N_2 molar ratio=2/8, (b-1) TGA profiles on the reduced catalysts after C_2H_6 dehydrogenation step, and (b-2) TGA profiles on the oxidized catalysts after subsequent CO_2 activation step.

(**Additional explanation**) In Fig. S7(a), the XPS peaks labelled with 'u' are assigned to Ce $3d_{3/2}$ spin-orbit states and those labelled with 'v' correspond to Ce $3d_{5/2}$ states [S1]. The peaks at the BEs of 885.8, 893.6, 897.9, 900.5, 907.0 and 916.3 eV are attributed to the Ce^{4+}, while the peaks at the BEs of 880.5, 884.9, 898.9 and 903.3 eV are associated with Ce^{3+}. The copresence of these characteristic peaks on the FeCe@Z suggests the coexistence of Ce^{4+} and Ce^{3+} ions over the catalyst surfaces. And the Ce^{4+} phases were reduced to the Ce^{3+} phases after C_2H_6 dehydrogenation (reduction step).

REFERENCES

S1. K. Kuntaiah, P. Sudarsanam, B. M. Reddy and A. Vinu, *RSC Adv.*, **3**, 7953 (2013).